



A study of long wave run-ups on a bi-linear beach slope induced by solitary and transient-focused wave group

Haeng Sik Ko & Patrick J. Lynett

To cite this article: Haeng Sik Ko & Patrick J. Lynett (2019) A study of long wave run-ups on a bi-linear beach slope induced by solitary and transient-focused wave group, Coastal Engineering Journal, 61:2, 135-151, DOI: [10.1080/21664250.2018.1558919](https://doi.org/10.1080/21664250.2018.1558919)

To link to this article: <https://doi.org/10.1080/21664250.2018.1558919>



Published online: 28 Dec 2018.



Submit your article to this journal [↗](#)



Article views: 105



View related articles [↗](#)





View Crossmark data [↗](#)



Citing articles: 2 View citing articles [↗](#)

A study of long wave run-ups on a bi-linear beach slope induced by solitary and transient-focused wave group

Haeng Sik Ko ^a and Patrick J. Lynett ^b

^aDepartment, Department of Ocean System Engineering, Jeju National University, Jeju, South Korea; ^bDepartment of Civil & Environmental Engineering, University of Southern California, Los Angeles, CA, USA

ABSTRACT

This paper presents long wave run-ups and rundowns on a bi-linear slope beach detected by using an image processing technique. For long wave run-ups, solitary wave run-up is obtained through experimental tests by Hydraulic-Control Wave-maker (HCW) and the dataset are validated by comparing Open-Source field Operation and Manipulation (OpenFOAM) with Reynolds Averaged Navier-Stokes (RANS)-type model and Cornell University Long and intermediate WAVE modelling package (COULWAVE) with Boussinesq-type model. For infragravity wave run-up, furthermore, a transient-focused wave group are generated and validated by the comparison of the numerical simulations. The results present not only that a low-frequency waves are enhanced by shoaling and breaking processes due to the bi-linear slope beach compare to the analytical solution on plane beach but that the series of wave run-ups are dominant by the low-frequency wave induced by the transient-focused wave groups.

ARTICLE HISTORY

Received 2 March 2018
Accepted 11 December 2018

KEYWORDS

Solitary wave; Hydraulic-Control Wave-maker (HCW); wave run-up; infragravity wave; a transient-focused wave group

1. Introduction

It is important to evaluate and predict wave run-up and inundation on slope because extreme events associated with them cause huge damages in the coastal area. Especially, the study of wave run-up by long waves is more essential because wave run-up and run-down in swash zone is dominant by long waves.

Studies for tsunami inundation or run-up, one of extreme events, have been widely performed by solitary wave in an experimental wave flume because the wave is easily generated or reproduced with single parameter, wave height. Synolakis (1987) studied linear and non-linear theories of solitary wave run-up on plane beaches and compared the theories with experimental results. He found that different run-up regimes of breaking and non-breaking solitary waves are existent. The maximum run-up law of non-breaking solitary wave was presented.

Kanoğlu and Synolakis (1998) investigated solitary wave run-up on piecewise linear topographies. They found asymptotic results with respect to solitary wave interaction with piecewise linear topographies in a counter-intuitive manner. For a composite slope beach, for instance, only a slope of closest to the shoreline affects the run-up. Li and Raichlen (2001) derived non-linear solution from shallow water equation, which includes higher-order terms than the solution derived by Synolakis (1987). Sælevik, Jensen, and Pedersen (2013) investigated and compared run-ups of solitary waves on

a straight and a composite beach. They thought that a relatively thinner run-up is created above vertex of the second slope than the straight slope.

On the other hands, the wave run-up is a summation of wave setup and swash motion. To understanding wave setup and swash oscillations composed of individual broken waves and infragravity waves is important for the beach environment. Guza and Thornton (1982) first discovered that swash oscillations have two components by spectral analysis. Hunt (1959) proposed a formula to predict wave run-up on open-coast beaches. Battjes (1974) rewrote the Hunt formula and suggested the dimensionless run-up as Iribarren number or surf similarity parameter (ξ) depending on an incoming wave condition and a beach slope.

$$\frac{R}{H_0} = \xi = \frac{\tan\beta}{\sqrt{H_0/L_0}} \text{ for } 0.1 < \xi < 2.3 \quad (1)$$

Where R is wave run-up, $\tan\beta$ is a beach slope, and H_0 and L_0 are the wave height and wave length in deep water, respectively.

If the surf similarity parameter is greater than 1.75, steep slopes or reflective beaches are classified. Otherwise, gentle slopes or dissipative beaches are called (Hunt, 2003). For steep slopes, incoming bores are more dominant than infragravity waves, whereas an effect of infragravity waves is bigger than incoming bores.

For dissipative slopes, wave setups become large in proportion to small swash motions since the wave setup is independent of the slope (Kobayashi, DeSilva, and Watson, 1989). In contrast, swash oscillations are bigger than wave setups on reflective slopes (Battjes, 1974).

It is important to measure wave run-up in an experimental wave flume, but the measurement is not easy because of the turbulence and aeration of the flow (Sælevik et al. 2013). A typical measurement of wave run-up is using serial wave gauges in a step-type array. Yet, the measurement has low resolution. A resistant-type run-up gauge parallel to a slope is often used, but the run-up is underestimated because of a distance between the run-up gauge and the slope. Recently a laser scanner has been used to detect water surface and wave run-up (Hofland et al., 2015). Pedersen et al. (2013) captured coloured wave run-up with a high-speed video camera and measured wave run-up with an edge detection method in MATLAB. In the image analysis method, an accuracy of data depends on an image quality. Moreover, when the wave retreats, the coloured wave becomes dim so that the capturing or detecting of wave rundown is difficult.

In this paper, the wave run-ups of solitary waves and top-hat spectral waves are investigated. The solitary wave and the top-hat spectral wave are for the study of tsunami run-up and infragravity wave run-up, respectively. An action camera cheaper than other measuring instruments is used for capturing and detecting the time series of shoreline movement by solitary waves and top-hat spectral waves with an edge detection method in MATLAB. In addition, wave rundowns are captured and detected by controlling an image contrast. The time series of wave run-ups are compared to numerical simulations with Open-Source field Operation and Manipulation (OpenFOAM) and Cornell University Long and intermediate WAVE modelling package (COULWAVE) to investigate an accuracy of the developed experimental measurement. Furthermore, the maximum run-up of solitary waves and top-hat spectral waves with various amplitudes measured is compared to numerical simulations. In the case of top-hat spectral waves, long wave generation in association with an interaction of a transient-focused wave group is based on the second-order wave theory (Longuet-Higgins and

Stewart, 1960) and the shoaling and breaking of the wave group on a composite slope by fast Fourier transform (FFT) are investigated. To investigate the space-time evolution of wave transformation and run-up, the contour plots of surface elevation and time series of wave run-up by the laboratory observation and the model predictions are illustrated. In addition, the space-time evolutions of low-frequency component of surface elevation and the time series of wave run-up by the laboratory observation and the model predictions to investigate the relationship between low-frequency wave and wave run-up are presented.

2. Laboratory experiment

2.1. Experimental set-up

The experiments were performed in the wave flume, 0.4 m of width, 0.6 m of height and 12 m of length. The still water depth was set at 0.38 m same as the top baffle height at an initial position during the experiments. The scale-up and improved Hydraulic-Control Wave-maker (HCW) (Ko and Lynett 2014) is located next to the end of flume to generate waves as shown in Figure 1. Two fixed baffles and one movable top baffle with 0.27 m of length are placed at the side of the flume and three pipe lines with 0.1 m diameter are connected to three paired cylinders as shown in Figure 2. To generate waves, flow rates via three baffles are controlled by piston movements in the cylinders and combinations of a screw-jack and a motor play a key role as a similar line actuator to move pistons. The mechanism is applied to the movable top baffle.

A composite beach is placed at the other side of the flume. The beach is made up of a relatively steep slope of 1:10 and relatively mild slope of 1:15 and the beach starts about 4.2 m from the baffle.

Water surface elevations were at fixed spatial locations were collected and measured from four surface piercing resistance wave gauges with a sampling frequency of 100 Hz. Two wave gauges were placed at a horizontal bottom and the other two wave gauges were located at the first slope and the second slope, respectively. The detailed wave flume set-up and wave gauge locations as seen in the Figure 1.

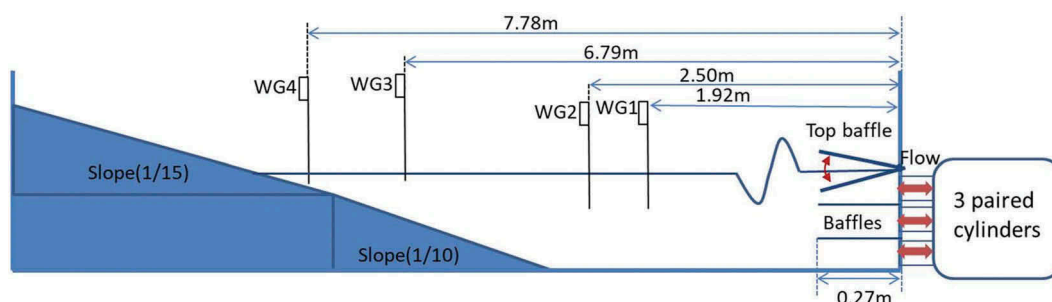


Figure 1. Schematic of wave flume and instrumentation.

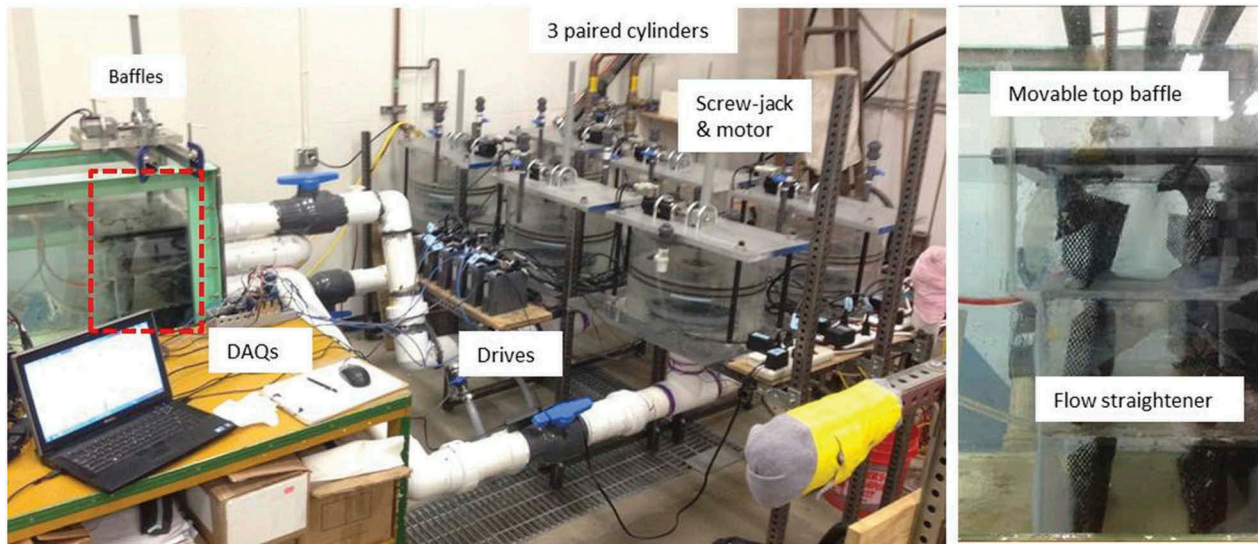


Figure 2. HCW with 3 paired cylinders (left) and a movable top baffle (right).

2.2. Wave run-up detection by image processing

Figure 3 shows the instrumental setup for detecting the time series of shoreline movement on x-direction. The rectangular structure built by perforated steel frames is positioned on slope, an area of interest. The frame is for covering the area by the light diffuser as seen in the Figure 3. If an image has glared spots due to a light, it makes the shoreline detection harder. An action camera with FHD resolution (1920 × 1080) and 30 fps is mounted on the right-hand side of the frame to cover overall the composite slope area. The composite slope is composed of a transparent plexiglass material so white PVC films are attached on the slope. Adhesive rulers are attached on the both sides of the slopes for using control points to transform local coordinate in image to global coordinate. Water is dyed with red food colouring. Among the edge detection methods, such as Roberts, Sobel, Prewitt, Canny, etc., the Canny edge detection is used in present paper. This is because the method is less sensitive to a noise in spite of more expensive than other methods (Kaur and Singh, 2016). The canny edge detection can be simply expressed as the following multi-step algorithm:

Step 1: Gaussian filtering to remove noise and unwanted details:

$$g(m, n) = \nabla[G(m, n) * f(m, n)] \quad (2)$$

where $G = \frac{1}{2\pi\sigma^2} e^{-\frac{m^2+n^2}{2\sigma^2}}$ as 2D isotropic Gaussian equation. m and n note image rows and columns, respectively. A filter size is that $(\sigma \times 3) \times 2 + 1$ is rounded to integer by neglecting the decimal part where a standard deviation (σ) is $\sqrt{2}$.

Step 2: Computing gradient of $g(m, n)$ and finding gradient angle ($\theta(m, n)$) using gradient operators:

$$M(n, n) = \sqrt{g_m^2(m, n) + g_n^2(m, n)} \quad (3)$$

$$\theta(m, n) = \tan^{-1}[g_n(m, n)/g_m(m, n)] \quad (4)$$

Step 3: Detecting an edge in the image based on gradient angle obtained in Step 3.

Step 4: Non-maximum suppression for tracing along the gradient in the edge direction and comparing the value perpendicular to the gradient.

Step 5: Hysteresis for eliminating streaking, which is breaking up of an edge caused by the operator output fluctuating above and below the threshold.

For the preprocessing, first, the video for monitoring shoreline movement was extracted to the sequence of image frames. The image frames have RGB colour as seen in Figure 4(a). The RGB images were masked except for area of interest to reduce analysing time and the images were converted to grayscale images for using edge detection in the Figure 4(b). Next, the grayscale images were analysed with *Canny edge* (Canny, 1986) function in MATLAB toolbox to detect shoreline movement. The function read the grayscale images to find edges and then outputs white pixel as the detected edge in black and white images in the Figure 4(c). The *canny edge* looks for local maximum values of the gradient of the grayscale images to find the edges so the setting appropriate threshold values in the gradient are important. *imopen* function in MATLAB toolbox carries out morphological opening on a grayscale image with a structuring elements. It makes that a relative small or weak noise in the grayscale images is filtered out before the edge detection. The Figure 4(d) shows the detected edges are overlapped on the RGB image.

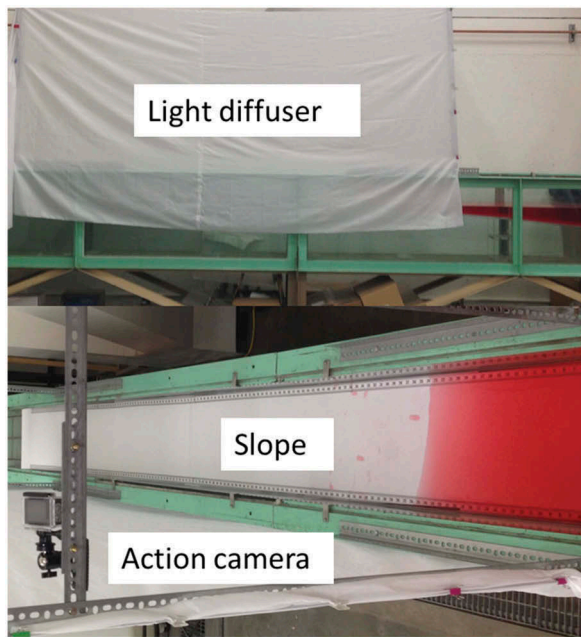


Figure 3. Side view (top) and top view (bottom) of instrumental setup.

The shoreline movement during wave run-up can be detected well by the image processing. However, it is difficult to detect the shoreline movement

during wave rundown. Water colour becomes faint and the faint water still leave on the composite slope even though wave is running down inner the faint water. To make the wave rundown more obvious, the image contrast in RGB images were controlled. **Figure 5** shows the comparison of *edge detection* without and with image contrast control during wave rundown.

During wave rundown, however, the faded colour sticks to the bottom of the slope due to added dye which leaves some water traces during wave rundown. To overcome the difficulty of the faded water traces, the following procedure is adopted to measure the exact wave rundown. Before the secondary successive wave run-up, the water has left out the traces on the slope beach, where it is more obvious to distinguish the shoreline and the traces. This will be taken as a reference trace and applied to each frame of the wave run-down and the unwanted matched edges will be removed by using image contrast control. In this paper, a contrast and a threshold value are manually controlled to reduce noise in image or the unwanted edges depending on conditions of each case.

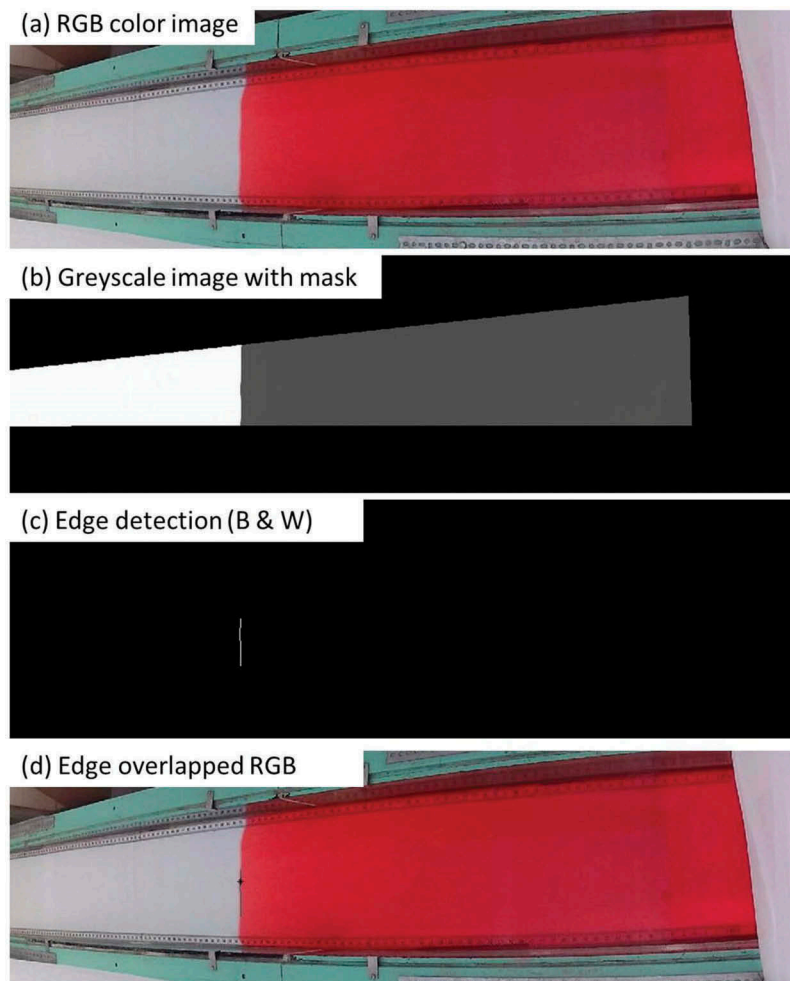


Figure 4. Process of edge detection. (a) RGB image; (b) Greyscale image with clipping mask; (c) Edge detection in black & white; (d) Edge overlapped RGB.

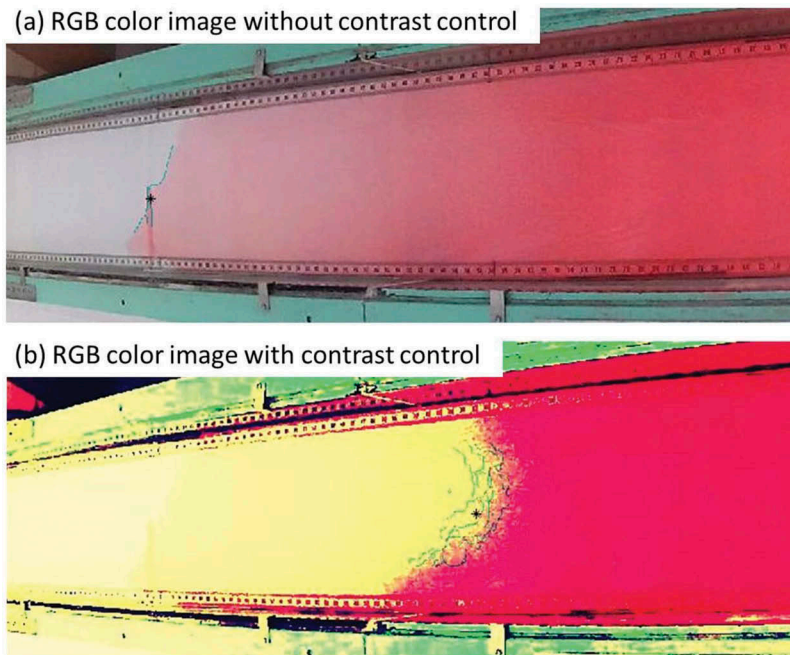


Figure 5. Comparison of edge detection without and with image contrast control during wave rundown.

2.3. Coordinate transformation

The process for coordinate transformation is similar to the process by Kalligeris et al. (2016).

First, the lens of the action camera with a fisheye lens for wide angles of view creates more distorted image of the Field Of View (FOV) than other cameras. The camera was calibrated with 13 check-board images including different angles of lens by using Caltch image calibration (Bouquet 1999) and the intrinsic parameters were obtained to remove the lens distortion. Secondly, local coordinates (u, v) in the image were transformed to global coordinates (x, y, z) by using Direct Linear Transformation (DLT) equation (Holland et al., 1997).

The set of collinearity equations is as follows:

$$\begin{aligned} u &= \frac{xL_1 + yL_2 + zL_3 + L_4}{xL_9 + yL_{10} + zL_{11} + 1}, \\ v &= \frac{xL_5 + yL_6 + zL_7 + L_8}{xL_9 + yL_{10} + zL_{11} + 1} \end{aligned} \quad (5)$$

where L_1, L_2, \dots, L_{11} are the DLT parameters.

Once the DLT coefficients are known, the global coordinates can directly be transformed to local coordinates in images as:

$$\begin{aligned} \begin{bmatrix} L_1 - L_9u & L_2 - L_{10}u & L_3 - L_{11}u \\ L_5 - L_9u & L_6 - L_{10}u & L_7 - L_{11}u \end{bmatrix} \begin{bmatrix} x \\ y \\ z \end{bmatrix} \\ = \begin{bmatrix} u - L_4 \\ v - L_8 \end{bmatrix} \end{aligned} \quad (6)$$

which gives a direct correspondence from local coordinates in images to global coordinates with $z = 0$, provided DLT parameters in Equation (7), are known.

$$\begin{bmatrix} x \\ y \end{bmatrix} = \begin{bmatrix} L_1 - L_9u & L_2 - L_{10}u \\ L_5 - L_9u & L_6 - L_{10}u \end{bmatrix}^{-1} \begin{bmatrix} u - L_4 \\ v - L_8 \end{bmatrix} \quad (7)$$

To calculate DLT parameters with the camera with ground control points, rewriting Equation (7) in the form $Ax = b$ with x is the vector as unknown DLT parameters.

$$\begin{bmatrix} x_i & y_i & 1 & 0 & 0 & 0 & -u_i x_i & -u_i y_i \\ 0 & 0 & 0 & x_i & y_i & 1 & -v_i x_i & -v_i y_i \end{bmatrix} \begin{bmatrix} L_1 \\ L_2 \\ L_4 \\ L_5 \\ L_6 \\ L_8 \\ L_9 \\ L_{10} \end{bmatrix} = \begin{bmatrix} u_i \\ v_i \end{bmatrix} \quad (8)$$

where (u_i, v_i) and (x_i, y_i) are known image and global coordinates with ground controls points.

At least four control points are needed to obtain eight DLT parameters. The more the control points are, the more accurate it is. 220 ground control points for a larger area of interest (for solitary wave run-up) and 164 ground control points for a smaller area of interest (for top-hat spectrum wave run-up) obtained by two measuring tapes attached on the sides of the flume for pairing the local in image and global coordinate are used.

The error ϵ_{xy} is calculated by the mean distance between the real (x, y) and predicted (x_p, y_p) coordinates:

$$\epsilon_{xy} = \frac{1}{N} \sum_{i=1}^N \sqrt{[x_p(i) - x(i)]^2 + [y_p(i) - y(i)]^2} \quad (9)$$

where N is the number of ground control points.

The mean error value for solitary wave run-up is 0.017 m and standard deviation is 0.40, whereas the mean error value for top-hat spectrum wave run-up is 0.005 m and standard deviation is 0.11. The error becomes bigger where ground control points are far from the

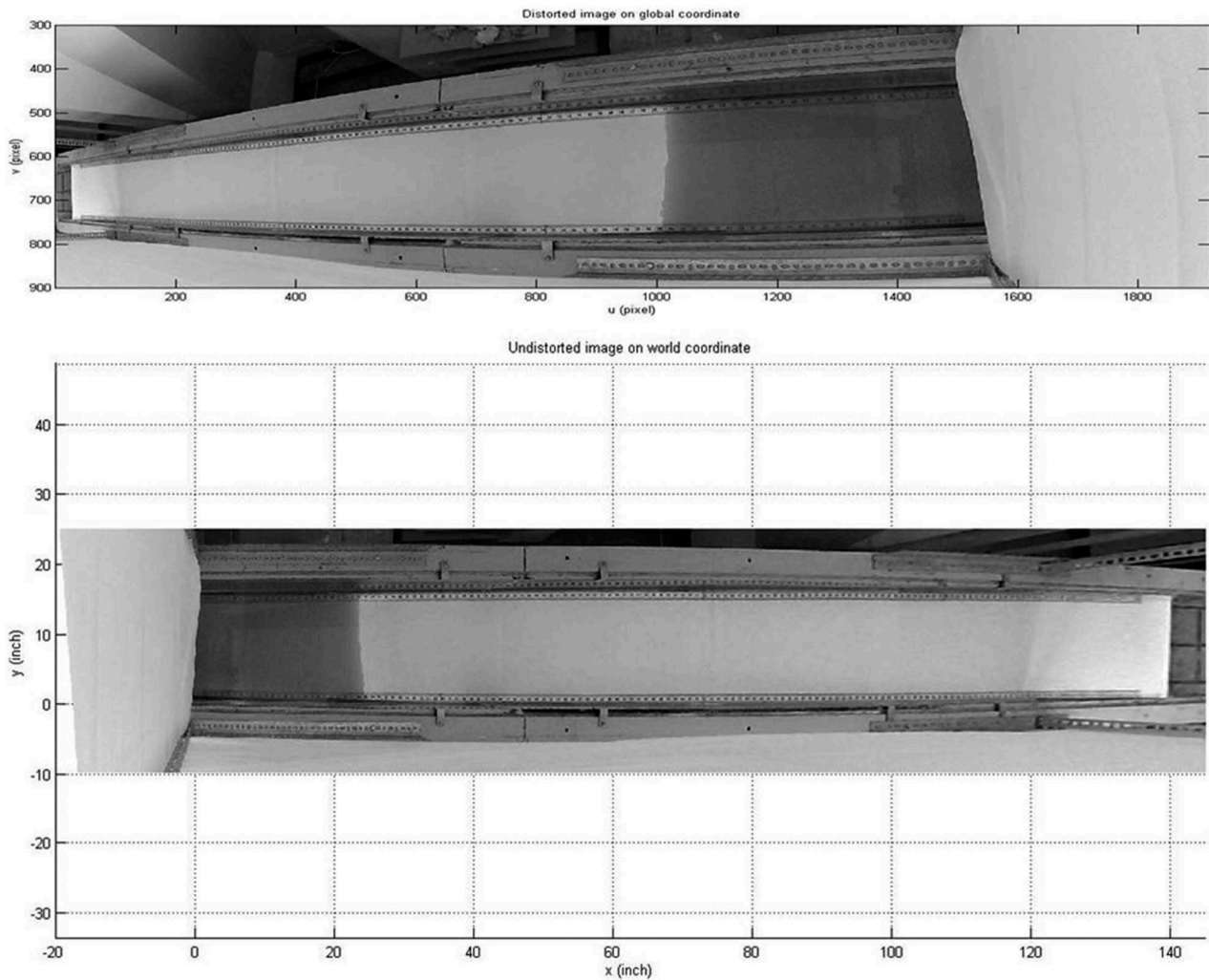


Figure 6. The distorted image (top) and the undistorted image with DLT transformation (bottom).

camera because the image resolution becomes low. The detection for solitary wave run-up is used many control points including the points are far from the camera because an area of interest to detect solitary wave run-up is bigger than top-hat spectrum wave run-up detection.

Once the DLT parameters are obtained, the detected points in local coordinates of images can be transformed to global coordinates by using Equation (7) considering local coordinated in undistorted image, as seen in Figure 6.

Although the process to reduce noises and to obtain clear edges was carried out, there are still noises from water drops during wave run-up and rundown. It is not an effective way to filter all noises from distributions of detected points. The median value of detected points was chosen with transformed coordinate to plot the time series of wave run-up.

3. Numerical models

3.1. OpenFOAM

The OpenFOAM is an open-source Computational Fluid Dynamics (CFD) software, and consists of C++ libraries

and codes that is used for creating applications including solvers or utilities (Weller et al., 1998). Solvers are each designed to solve a specific problem in continuum mechanics, and utilities are designed to perform tasks that involve data manipulation. The package distribution enables us to use numerous solvers and utilities and to write our own solver that is suitable for our desired problem, but a solid knowledge of physics and programming is needed. In this study, the *interFoam* solver is used, which is the solver for multiphase problems with incompressible fluids.

3.1.1. Governing equations

Navier-Stokes equation for an incompressible flow and constant viscosity is:

$$\frac{Du}{Dt} \equiv \frac{\partial u_i}{\partial t} + u_j \frac{\partial u_i}{\partial x_j} = -\frac{1}{\rho} \frac{\partial p}{\partial x_i} + \nu \frac{\partial^2 u_i}{\partial x_j^2} \quad (10)$$

where $x_{i,j}$ ($i, j = 1, 2, 3$) are Cartesian coordinates, u_i are the Cartesian components of the velocity, while t represents the time, ρ is the density of the fluid, p is the pressure, g is the acceleration of gravity, and ν is the fluid dynamic viscosity.

The continuity equation for an incompressible flow must also be satisfied:

$$\frac{\partial \bar{u}_j}{\partial x_j} = 0 \quad (11)$$

The Reynolds Averaged Navier-Stokes (RANS) equations are time-averaged equations used to analyse turbulent flows. The continuity (Equation (12)) and momentum (Equation (13)) equations for an incompressible fluid can be written, using Einstein summation convention as:

$$\frac{\partial \bar{u}_j}{\partial x_j} = 0 \quad (12)$$

$$\frac{\partial \bar{u}_i}{\partial t} + \bar{u}_j \frac{\partial \bar{u}_i}{\partial x_j} = -\frac{1}{\rho} \frac{\partial}{\partial x_j} \left[\bar{p} \delta_{ij} - \mu \left(\frac{\partial \bar{u}_i}{\partial x_j} + \frac{\partial \bar{u}_j}{\partial x_i} \right) + \rho \overline{u'_i u'_j} \right] \quad (13)$$

where \bar{u}_j is the time-averaged velocity and δ_{ij} is Kronecker delta function.

The relationship of the turbulent-viscosity hypotheses to analyse the stress-rate-of-strain relation for a Newtonian fluid is

$$-\overline{u'_i u'_j} = \nu_T \left(\frac{\partial \bar{u}_i}{\partial x_j} + \frac{\partial \bar{u}_j}{\partial x_i} \right) - \frac{2}{3} k \delta_{ij} \quad (14)$$

where ν_T is the turbulent viscosity. The turbulent-viscosity hypothesis substituted into the momentum of RANS (Equation (13)) is

$$\frac{\partial \bar{u}_i}{\partial t} + \bar{u}_j \frac{\partial \bar{u}_i}{\partial x_j} = \frac{\partial}{\partial x_j} \left[\nu_{eff} \left(\frac{\partial \bar{u}_i}{\partial x_j} + \frac{\partial \bar{u}_j}{\partial x_i} \right) \right] - \frac{1}{\rho} \frac{\partial}{\partial x_i} \left(\bar{p} + \frac{2}{3} \rho k \right) \quad (15)$$

where ν_{eff} is the effective viscosity, which takes into account the summation of the molecular viscosity (ν) and the turbulent viscosity (ν_t), and k is turbulent kinetic energy.

3.1.2. The $k - \epsilon$ model

The two-equation $k - \epsilon$ turbulence model is one of the most common turbulence models. The equation solves the turbulent kinetic energy (k) and the dissipation rate of the turbulent kinetic energy (ϵ) to represent turbulent properties such as convection and diffusion of turbulent energy. The model is widely used for most types of engineering applications. The modelled transport equations for k and ϵ are:

$$\frac{\partial k}{\partial t} + \bar{u}_j \frac{\partial k}{\partial x_j} = \frac{\partial}{\partial x_j} \left[\left(\nu + \frac{\nu_t}{\sigma_k} \right) \frac{\partial k}{\partial x_j} \right] + \nu_t \left(\frac{\partial \bar{u}_i}{\partial x_j} + \frac{\partial \bar{u}_j}{\partial x_i} \right) \frac{\partial \bar{u}_i}{\partial x_j} - \epsilon \quad (16)$$

$$\frac{\partial \epsilon}{\partial t} + \bar{u}_j \frac{\partial \epsilon}{\partial x_j} = \frac{\partial}{\partial x_j} \left(\frac{\nu_t}{\sigma_\epsilon} \frac{\partial \epsilon}{\partial x_j} \right) + C_{\epsilon 1} \frac{\epsilon}{k} \nu_t \left(\frac{\partial \bar{u}_i}{\partial x_j} + \frac{\partial \bar{u}_j}{\partial x_i} \right) \frac{\partial \bar{u}_i}{\partial x_j} - C_{\epsilon 2} \frac{\epsilon^2}{k} \quad (17)$$

where turbulent viscosity is given by $\nu_t = C_\mu k^2 / \epsilon$, and σ_k and σ_ϵ are the turbulent Prandtl number for k and ϵ , and C_μ , $C_{\epsilon 1}$ and $C_{\epsilon 2}$ are model constants. The standard $k - \epsilon$ model constants in the model equations are: $\sigma_k = 1.0$, $\sigma_\epsilon = 1.3$, $C_\mu = 0.09$, $C_{\epsilon 1} = 1.44$, $C_{\epsilon 2} = 1.92$.

3.1.3. Volume of fluid method

In OpenFOAM, the VOF (Volume of Fluid) method is used for tracking interface movement between air and water. The equation determines volume fraction, but the sharpness interface can possibly become smeared due to false diffusion (Versteeg and Malalasekera, 2007). In OpenFOAM, an extra term called artificial compression is introduced into the phase fraction equation:

$$\frac{\partial \alpha}{\partial t} + \nabla \cdot (\alpha U) + \nabla \cdot (\alpha(1 - \alpha)U_r) = 0 \quad (18)$$

where U is the velocity field composed of u , v and w , and α is the phase fraction of water and air. $\alpha = 1$ and $\alpha = 0$ mean that a cell is full of water and air, respectively. The artificial compression velocity in OpenFOAM can be controlled by *cAlpha*. For no compression velocity, *cAlpha* set to zero value, and higher values than zero mean that an artificial velocity at the interface is applied.

The phase fraction α determines the density of mixture in the Navier-Stokes equations. The equation is as follows:

$$\rho = \alpha \rho_w + (1 - \alpha) \rho_a \quad (19)$$

where ρ_w and ρ_a represent the density of water and air, respectively.

3.1.4. OpenFOAM with a movable top baffle

The *interDyMFoam* solver is combination of the *interFoam* solver and a dynamic mesh motion is used for a simulation of top baffle movement. For the dynamic mesh motion, one of mesh motion methods in OpenFOAM, *dynamicMotionSolverFvMesh*, is used, and requires a cell motion equation and a diffusivity model. The cell motion equation, *displacementLaplacian*, is based on the Laplacian of the diffusivity and needs a *pointDisplacement* file at initial time. For the diffusivity model, *inverseDistance* is used, and makes that the points after solving the cell motion equation can be moved by the diffusivity of the field based on the inverse distance from boundaries. With the solver, a dynamic mesh motion with 6 DOF (Degrees Of Freedom) can be simulated. In this study, 1 DOF, a rotation on z-axis is only considered to simulate a movable top baffle. The time series of rotations on z-axis are calculated depending on the

time series of water surface elevation and obtained as input data for the top baffle movement. In the numerical simulation, the time-varying volume of top baffle same as the experiment are considered.

3.1.5. Numerical conditions of OpenFoam

For numerical simulation, grid sizes of 0.019 m on horizontal direction and 0.006 m on vertical direction are chosen, which are around 6–15 grids per wave heights and 141–378 grids per wave length. The number of grid per wave height and length is determined based on Ko, Bae, and Cho (2018). An adjustable time step which means that a time step is calculated for satisfying Courant–Friedrichs–Lewy (CFL) condition every time step is used. Non-slip boundary condition is applied on wall and slope beach. For generating waves, the time series of input velocity are calculated based on analytical solutions and imposed in each inlet boundary condition which is same as the experimental HCW.

3.2. COULWAVE

COULWAVE is based on the expanded Boussinesq equation with some modifications by weakly dispersive terms (Madsen and Sorensen, 1992) and highly non-linear free surface disturbances (Liu, 1994; Wei et al., 1995). The COULWAVE including a moving boundary treatment has shown to give good predictions with respect to wave run-up (Lynett, Wu, and Liu, 2002). The continuity and momentum equations of the model are given in dimensional form:

$$\begin{aligned} & \eta_t + \nabla \cdot (Hu_a) - \nabla \\ & \cdot \left[H \left\{ \frac{1}{6} (\eta^2 - \eta h + h^2) - \frac{1}{2} z_a^2 \right\} \nabla (\nabla \cdot u_a) \right] \\ & - \nabla \cdot \left[H \left\{ \frac{1}{2} (\eta h - h) - z_a \right\} \nabla (\nabla \cdot (hu_a)) \right] \\ & = 0 \end{aligned} \quad (20)$$

$$\begin{aligned} & u_{at} + u_a \cdot \nabla u_a + g \nabla \eta + \left[\frac{z_a^2}{2} \nabla (\nabla \cdot u_{at}) + z_a \nabla (\nabla \cdot (hu_{at})) \right] \\ & + [(\nabla \cdot (hu_a)) \nabla (\nabla \cdot (hu_a)) - \nabla (\eta (\nabla \cdot (hu_{at})))] \\ & + (u_a \cdot \nabla z_a) \nabla (\nabla \cdot (hu_a)) \\ & + \left[z_a (u_a \cdot \nabla z_a) \nabla (\nabla \cdot u_a) + \frac{z_a^2}{2} \nabla \{ u_a \cdot \nabla (\nabla \cdot u_a) \} \right] \\ & + \nabla \left[\frac{\eta^2}{2} \nabla \cdot u_{at} - \eta u_a \cdot \nabla (\nabla \cdot (hu_a)) + \eta (\nabla \cdot (hu_a)) \nabla \cdot u_a \right] \\ & + \nabla \left[\frac{\eta^2}{2} \{ (\nabla \cdot u_a)^2 - u_a \cdot \nabla (\nabla \cdot u_a) \} \right] = 0 \end{aligned} \quad (21)$$

where η is the free surface elevation and h is the local water depth. u_a is the reference velocity vector at the elevation $z_a = -0.531h$ recommended by Nwogu (1993). The first and second terms in the left-hand side of continuity equation (Equation 20) and the

first, second and third terms in the left-hand side of momentum equation (Equation 21) are given by the linearized Boussinesq and shallow water equation. Otherwise, the other terms are introduced by the expanded Boussinesq-type derivation. All waves are generated at a source location same as the end of baffle of experiment. The top-hat spectral waves are generated without a sponge layer for the same condition as the experiment. For the numerical simulation a grid size of 0.02 m and time step of 0.01s are used based on Lynett, Wu, and Liu (2002). Bottom friction is neglected.

4. Wave generation

4.1. Solitary wave

In this study, the free surface elevation (η), horizontal particle velocity (u) and vertical particle velocity (w) for solitary wave theory are adapted from Daily and Stephan (1952).

$$\eta = a \operatorname{sech}^2 \sqrt{\frac{3a}{4h^3}} (x - ct) \quad (22)$$

$$u = \sqrt{\frac{g}{h}} \left[\eta - \frac{\eta^2}{4h} + \left(\frac{h^2}{3} - \frac{z^2}{2} \right) \frac{\partial^2 \eta}{\partial x^2} \right] \quad (23)$$

$$w = -z \sqrt{\frac{g}{h}} \left[1 - \frac{\eta}{2h} \frac{\partial \eta}{\partial x} + \frac{h^2}{3} + \frac{z^2}{2} \frac{\partial^3 \eta}{\partial x^3} \right] \quad (24)$$

Where the wave celerity is given by $c = \sqrt{gz(1 + a/z)}$ is wave celerity and z is vertical coordinate.

4.2. Top-hat spectrum wave

In this study, transient-focused wave groups composed of 50 primary wave components with a same amplitude were generated because the top-hat spectral wave are transformed to long wave and the propagation path can be observed directly. The primary wave components were uniformly spaced over two different frequency bandwidths to obtain “top-hat” frequency spectra (Rapp and Melville, 1990). Total wave group amplitude, A , the frequency bandwidth, Δf , and the central frequency, f_c , are defined as

$$A = \frac{H}{2} = a_n N; \Delta f = f_1 - f_N; f_c = \frac{1}{2} (f_1 + f_N) \quad (25)$$

where a_n is the amplitude of the n th frequency component and N is the number of individual wave components.

The surface elevation of top-hat spectrum, η , is given by summation of linear wave components as follows:

$$\eta(x, t) = \sum_{n=1}^N a_n \cos(k_n x - \sigma_n t) \quad (26)$$

Table 1. Wave group conditions.

Case	Δf	f_c	f_1	f_N	T_g	a/h
A	0.167	0.75	0.833	0.667	12	0.0452
B	0.167	0.75	0.833	0.667	12	0.0812
C	0.167	0.75	0.833	0.667	12	0.1207

where k_n and σ_n are wave number and wave frequency of the n th wave component, respectively.

The six cases with same frequency bandwidths by Lara, Ruju, and Losada (2010) were examined as seen in Table 1.

The top-hat spectral waves are periodic with period $T' = N/\Delta f$ so that the wave signals are truncated in time to obtain a single wave group signal (Rapp and Melville, 1990). The time is decided by $T_g = 2/\Delta f$, the minimum value of the period of the wave packets at focal point. The practical reason makes that the "top-hat" spectral shape is transformed to "Sombrero (Mexican) hat" spectral shape. The number of waves in the groups is obtained by $N_w = 2f_c/\Delta f$. The detailed wave group conditions are summarized in Table 1.

In this paper, for generating waves in the experiment and OpenFOAM, the horizontal velocity profile from the analytical solution is integrated over 3 baffle inlets and the time series of input flow rates for the experiment and time series of input velocities for OpenFOAM are applied to flow rate systems and inlets, respectively. For wave generations in COULWAVE simulation, a source location is same as the end of baffle of experiment. In the case of solitary wave, a sponge layer is located at the opposite of wave propagation, while the top-hat spectral wave is generated without a sponge layer to predict a bounding long wave motion same as the experiment. Figure 7 presents comparisons of solitary wave with $a/h=0.12$ and top-hat spectral wave with C case surface elevations time series between experimental data and numerical results by COULWAVE and OpenFOAM at WG1. Furthermore, the maximum wave amplitudes of all cases from the experimental data, COULWAVE and OpenFOAM at WG1 are described in Table 2. The comparisons show that incident waves between the experiment and the numerical simulation before wave run-up the sloping beach are closely same.

5. Results and analysis

5.1. Solitary wave run-up

Figure 8 presents the comparison of the time series of solitary wave inundations and run-ups with $a/h=0.06$ and 0.12 measured and predicted with COULWAVE and OpenFOAM. The time series of run-up height was obtained by multiplying inundation length and $\sin(\tan^{-1}(m_2))$, where m_2 is the second slope from offshore.

The time series of inundations and wave run-ups measured are in close agreement with the predictions

by numerical simulations, COULWAVE and OpenFOAM. In detailed discrepancies between observations and predictions, the predictions with COULWAVE are faster rundown than the prediction with OpenFOAM and the measurements. This reason is that the predictions with COULWAVE may not be fully dispersive in very shallow region over the composite slope due to the inherent characteristics. On the other hands, the predictions with OpenFOAM with relatively small wave amplitudes ($a/h=0.06$) are good agreement with the measurements. However, the predictions with OpenFOAM with relatively high wave amplitudes ($a/h=0.12$) are higher wave run-ups and more abnormal path of wave run-ups and rundowns such as near $t=13$ and 15 s than the experiments. The reason results from inherent characteristics of VOF scheme difficult to track an exact free surface elevation in strong interaction area between air and water phase. In the simulation of solitary wave with $a/h=0.12$, water bubbles over the composite slope are observed during the maximum wave run-up and the minimum rundown. The second run-ups by the reflected solitary wave measured are in close agreement with the OpenFOAM. Yet, the predictions with COULWAVE are different because a sponge layer is located at the opposite of wave propagation as mentioned earlier.

The comparison of maximum solitary wave run-ups between model predictions and experimental data are shown in Figure 9. The maximum experimental run-ups are expressed as the median values of the detected maximum run-ups and the errors between maximum and minimum values of the detected maximum run-ups. The predictions are in close agreement with the solid line which means perfect agreement with the experiments.

5.2. Top-hat spectrum wave

5.2.1. Free surface and long wave elevation

Figure 10 shows the measured (solid line) and the predicted (dashed line) total wave elevation (blue) and long wave elevation (green) time series at different cross-shore location for case C. Long-wave components were obtained from low-pass filtered surface elevations by time-series measurement and cut-off frequency of $f_c < 0.4$ Hz.

In offshore, in the locations of WG1 and WG2, the bound long wave beneath the group is clearly visible and the scale of the long wave is 5 times magnification of the right-hand vertical scale. In the locations of WG3, single large wave in the group makes wave energy-focused (Rapp and Melville, 1990; Baldock, Swan, and Taylor, 1996). The bound long wave and the positive surge in advance of the short wave groups are enhanced by short-wave focusing and shoaling. The negative pulse after the bound long wave is identified as the radiated long wave from

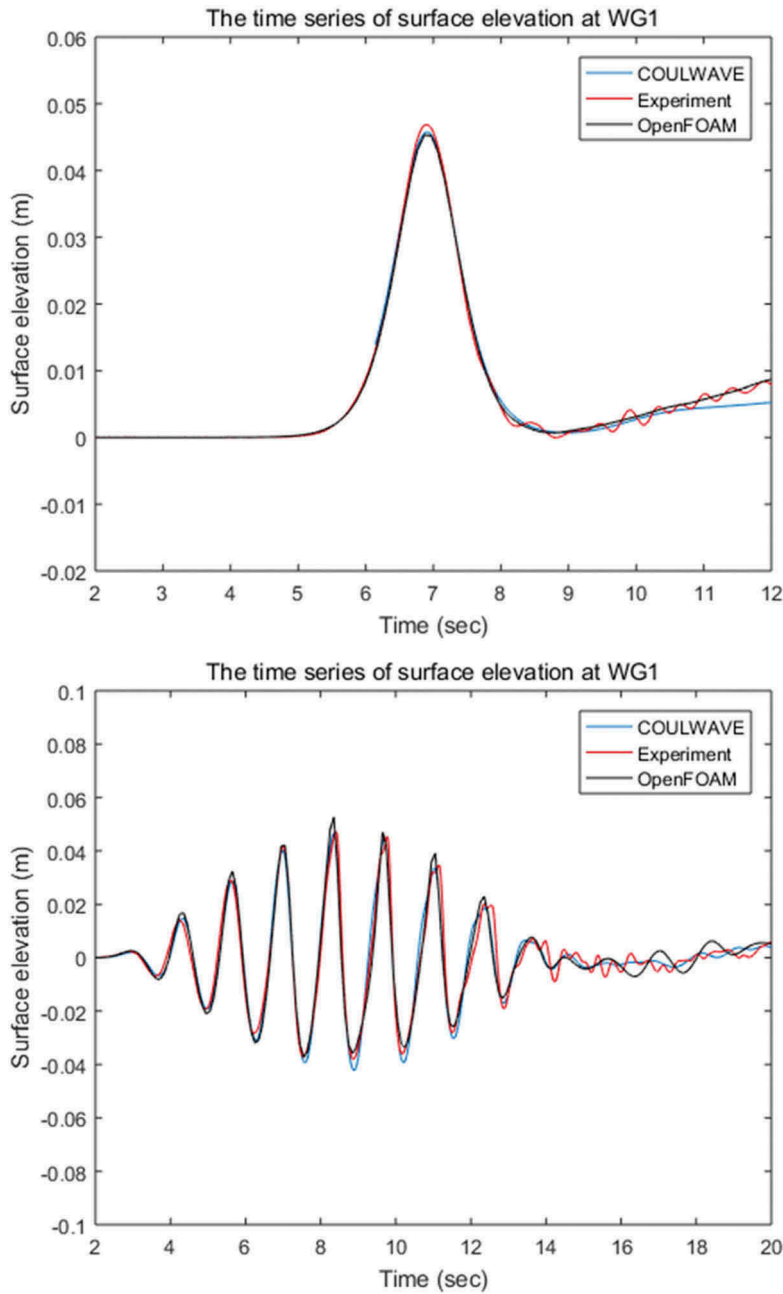


Figure 7. Comparisons of solitary wave with $a/h = 0.12$ (top) and Case C of top-hat spectrum wave (bottom) surface elevations time series at WG 1. Blue: model prediction by COULWAVE, Green: model prediction by OpenFOAM, Red: experimental data.

Table 2. Comparison of maximum solitary and top-hat spectrum wave amplitude at WG1.

Case	Target a/h	Experiment (a/h)	COULWAVE (a/h)	OpenFOAM (a/h)
Solitary	0.0600	0.0600	0.0600	0.0595
	0.0700	0.0699	0.0701	0.0694
	0.0800	0.0804	0.0802	0.0794
	0.0900	0.0894	0.0902	0.0893
	0.1000	0.1006	0.1003	0.0993
	0.1100	0.1121	0.1103	0.1093
	0.1200	0.1233	0.1204	0.1193
Top-hat A	0.0452	0.0442	0.0445	0.0445
Top-hat B	0.0812	0.0787	0.0786	0.0770
Top-hat C	0.1207	0.1120	0.1170	0.1184

the breakpoint. In the locations of WG4, the surging motion is more dominant than bounding wave in numerical simulations. As the exact surface elevation with a resistance wave gauge (WG4) located in extremely shallow water depth could have been measured erroneously, and also the numerical simulations are expected to dissipate less energy after wave breaking. To affirm the above statement further investigation is required, however, it has been left out in the present study. Moreover, it is observed that the bounded long wave and the positive wave surge in advance the wave groups are amplified and reach their maximum wave height in shallow water.

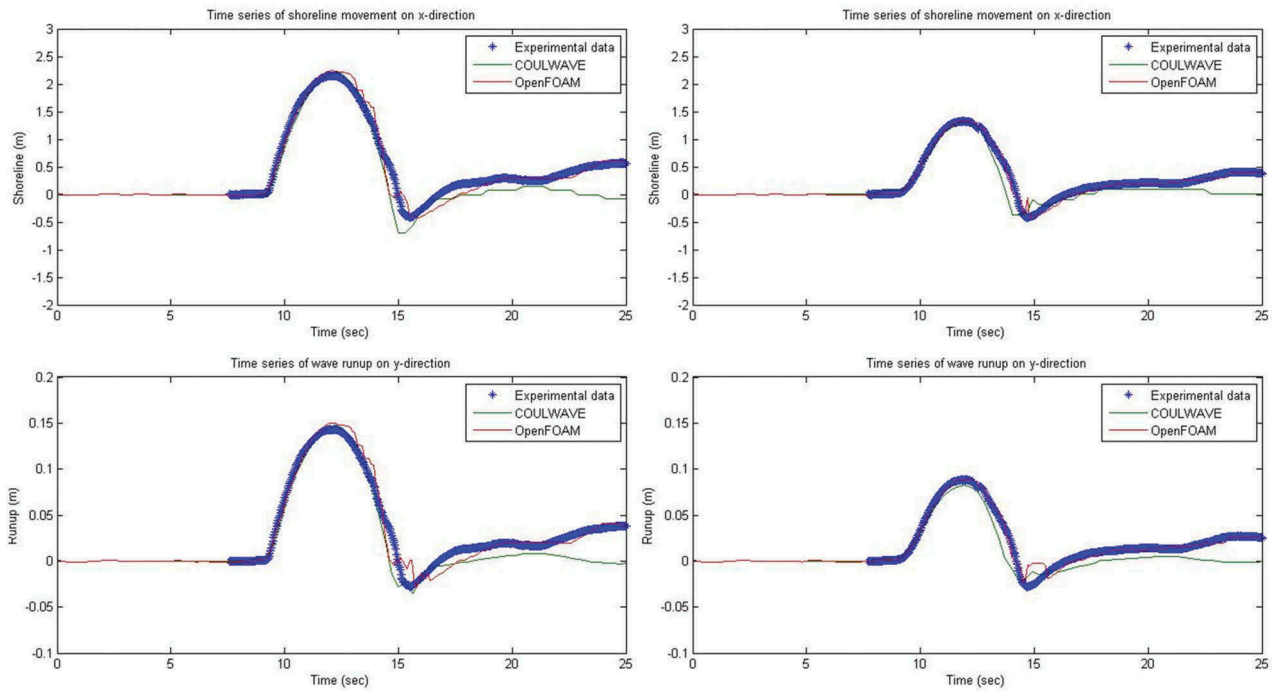


Figure 8. Comparison of the time series of solitary wave inundation (top) and run-up (bottom) with $a/h = 0.06$ (left column) and 0.12 (right column). Asterisk: experimental data, green: COULWAVE, red: OpenFOAM.

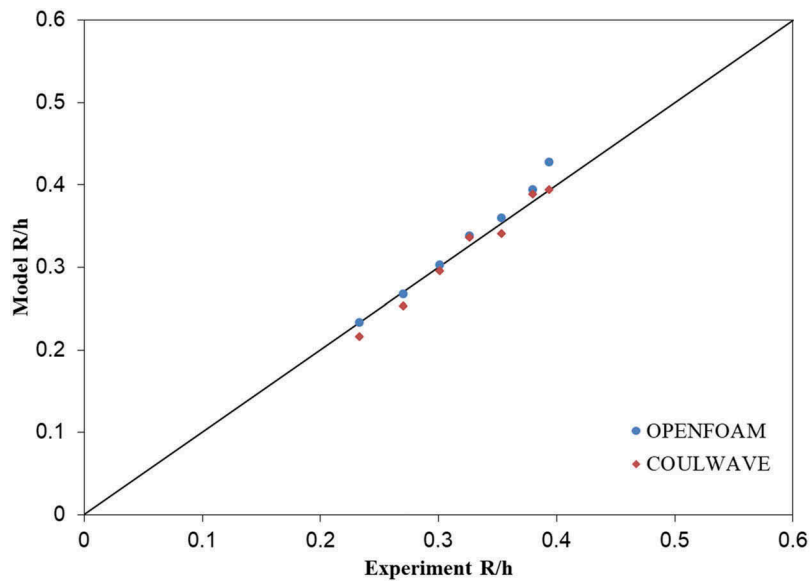


Figure 9. Comparison of maximum solitary wave run-up between experiment and model predictions. Blue circle: OpenFOAM, red diamond: COULWAVE, solid line: perfect agreement.

5.2.2. Wave amplitude spectrum

Using the solution procedure by Stokes (1847), Longuet-Higgins and Stewart (1960) proposed that the second-order solutions of water surface elevation (η) and velocity potential (ϕ) considering the interaction between two progressive waves are:

$$\eta = \eta_1 + \eta_2 + \frac{a_1 a_2}{2g} [C \cos(\psi_1 - \psi_2) - D \cos(\psi_1 + \psi_2)] \quad (27)$$

where the subscripts denote each progressive wave, and η_1 , η_2 , ϕ_1 , and ϕ_2 are the first approximations of water surface elevation and velocity potential

expressed in terms of the phase angle is given by $\psi = kx - \sigma t$, and a , k , and σ are wave amplitude, the wave number and the wave frequency, respectively. The coefficients of second-order solutions (C , D , E , and F) defined by Longuet-Higgins and Stewart (1960) are reproduced in Appendix A.

The term of $\psi_1 - \psi_2$ is associated with the global or low-frequency interaction, whereas the term of $\psi_1 + \psi_2$ corresponds to the local non-linear interaction.

To apply the Equations (24) and (25) to a focused wave group, Baldock, Swan, and Taylor (1996) introduced a summation of the interactions due to each

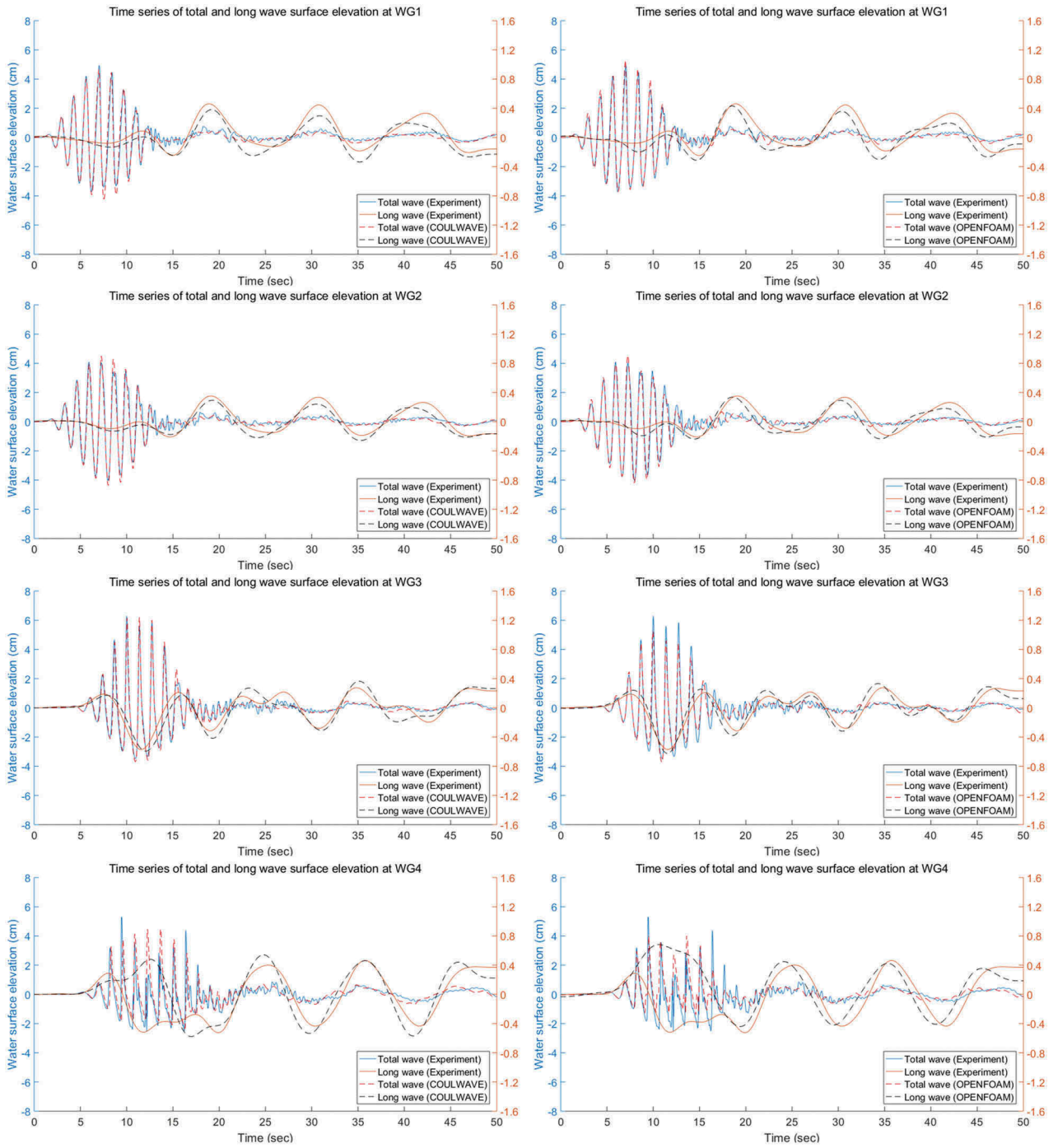


Figure 10. Time series of total (blue) and long wave elevation (green) of case C. Solid line: experiment; dashed line: OpenFOAM (left column) and COULWAVE (right column).

pair of wave components and produced a - total second-order solution. The second-order solutions of the water surface elevation and the velocity potential are respectively expressed as

$$\eta = \sum_{n=1}^N \eta(n) + \sum_{n=1}^N \sum_{m=n+1}^N \eta(n, m) \quad (29)$$

$$\phi = \sum_{n=1}^N \phi(n) + \sum_{n=1}^N \sum_{m=n+1}^N \phi(n, m) \quad (30)$$

where η_n and ϕ_n are the first approximations of water surface elevation and velocity potential for the n th wave component, and $\eta(n, m)$ and $\phi(n, m)$ are the second-order interactions between n th and m th wave components. The terms with respect to the interactions for the paired waves are calculated by using the Equations (29) and (30). The analytical solutions will be compared to the laboratory data and the numerical results.

Figure 11 shows the surface elevation amplitude spectra with different wave amplitudes at different

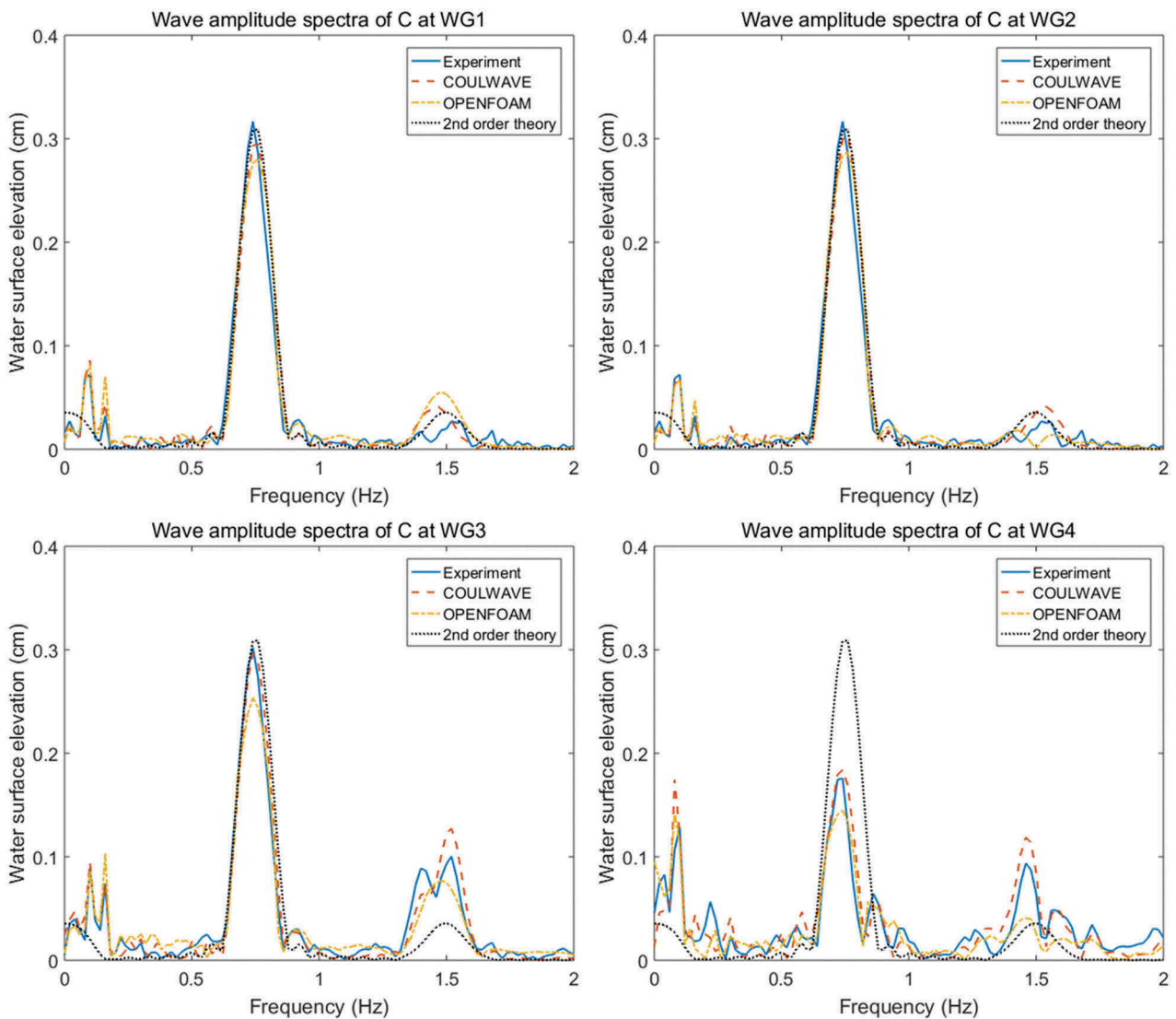


Figure 11. Amplitude spectra of case C. Blue: experiment; dashed green: model predictions by COULWAVE; dashed-dot red: model prediction by OpenFOAM; second-order theory at wave-maker position ($x = 0$).

cross shore locations for case C. The laboratory data (solid line) are compared to the numerical results with OpenFOAM (dashed-dot line) and COULWAVE (dashed line) and the second-order solution (dotted line) by Longuet-Higgins and Stewart (1960). In addition, the amplitude spectra of the second-order solution are predicted at the wave-maker position ($x = 0$). The comparisons of the theory at initial location and experimental data and numerical results at various cross shore locations present that a spatial redistribution of wave energy is obviously described during the shoaling and breaking processes. The wave amplitude spectra in WG1 of all cases measured and predicted shows the primary short wave amplitude in the frequency range ($0.7 \text{ Hz} < f < 0.8 \text{ Hz}$) and the second-order superharmonics in the frequency range ($1.4 \text{ Hz} < f < 1.6 \text{ Hz}$) are in close agreement with the second-order wave theory by Longuet-Higgins and Stewart (1960). In contrast, the bound long wave subharmonics in the frequency range ($f < 0.2 \text{ Hz}$) measured and predicted are different with the second-order wave theory. The

additional radiations of the energy at shoreward for long wave generation, such as shoaling and breaking processes are required (Baldock, 2006). The wave amplitude spectra in the superharmonic band frequency measured and predicted in WG3 and WG4 are more increased than the second-order theory due to the wave shoaling on the composite sloping beach. Moreover, the wave amplitude spectra in the primary short wave group band frequency measured and predicted in WG4 more decreased than the second-order solution because of wave breaking.

The wave amplitude spectra with low-frequency increase over nearshore regions because the wave amplitudes with low-frequency become increased in shallow water due to wave shoaling and the energy is transferred from the waves with higher frequency.

5.2.3. Top-hat spectrum wave run-up

Figure 12 presents the comparison of the time series of inundations and run-ups of top-hat spectral waves

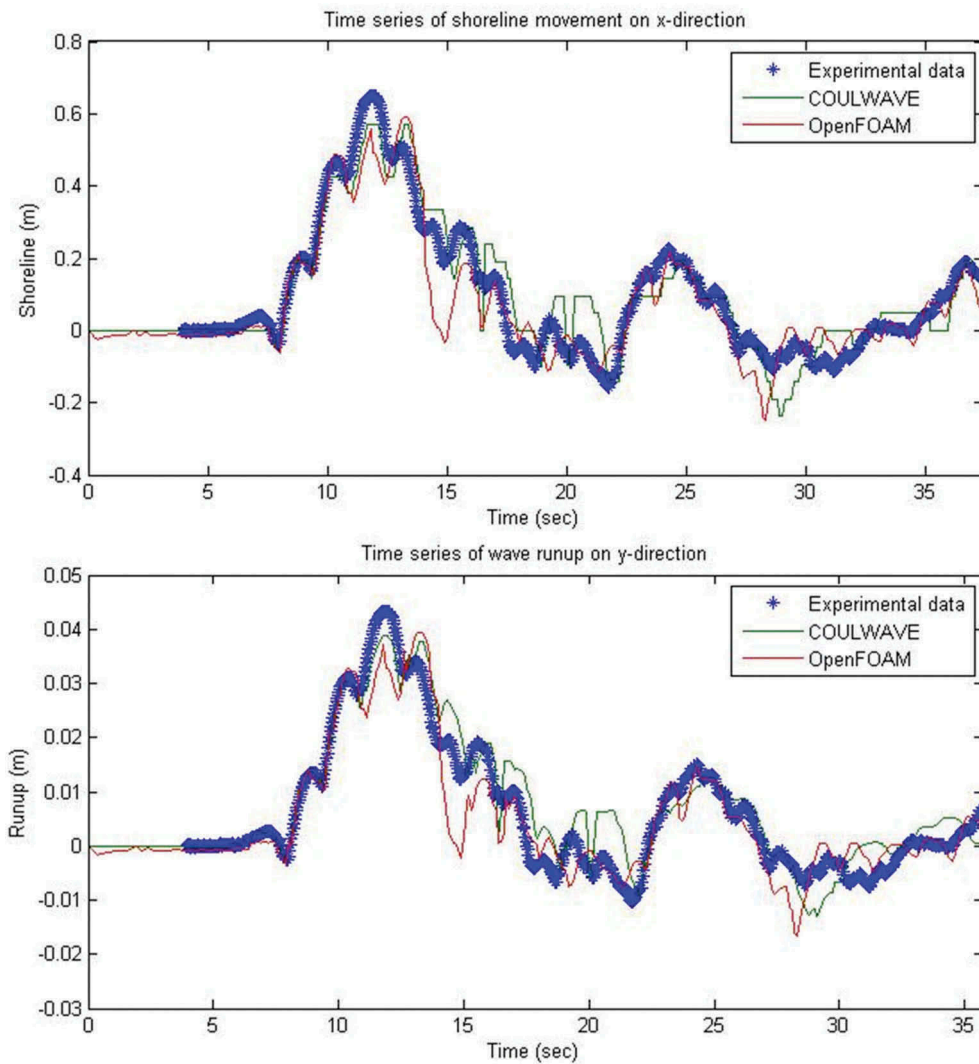


Figure 12. Comparison of the time series of top-hat spectrum wave inundation (top) and run-up (bottom) with case C. Asterisk: experimental data, green: COULWAVE, red: OpenFOAM.

(case C) measured and predicted with COULWAVE and OpenFOAM. The time series of run-up height is obtained by multiplying inundation length and $\sin(\tan^{-1}(m_2))$, where m_2 is the second slope from offshore. The time series of inundations and wave run-ups for all cases measured and predicted with COULWAVE and OpenFOAM have discrepancies because the wave conditions at WG4 are also different as described in the section 6.1. However, the tendencies of wave run-ups and rundowns are so close between the measurements and the predictions. It is observed that the sequence of wave run-ups by the bounded long wave contains high-frequency oscillations in the time series. The time series of run-ups with numerical simulations at 15 s are under-predicted compared to the experiments. The time series of water surface elevations with numerical simulations are under-predicted at the end of wave packet period ($t = 16\text{--}17$ s) as shown in the Figure 10.

The Figure 13 presents the space-time evolution of low-frequency component ($f_c < 0.4$) of surface elevation and the time series of wave run-up by the laboratory

observation (top), OpenFOAM (middle) and COULWAVE (bottom) of case C. The figure shows that the bound long wave is amplified by shoaling after passing the first slope and that the subsequent wave run-ups are dominated by the reflected bound long wave. The figure obviously shows that the subsequent wave run-ups are dominated by the reflected bound long wave. The positive surges in advance of bound long wave trough lead a low-frequency run-up on the composite slope.

6. Conclusions

In this paper, the measurement for wave run-up were performed with images captured by using the one action camera, food colourings, light diffuser materials low costs as well as *edge detection* function in MATLAB toolbox. In addition, wave rundown could be detected by controlling image contrast.

In solitary waves with various amplitudes, the time series of inundations and wave run-ups and wave rundowns measured are in close agreement with the predictions by numerical simulations, COULWAVE and

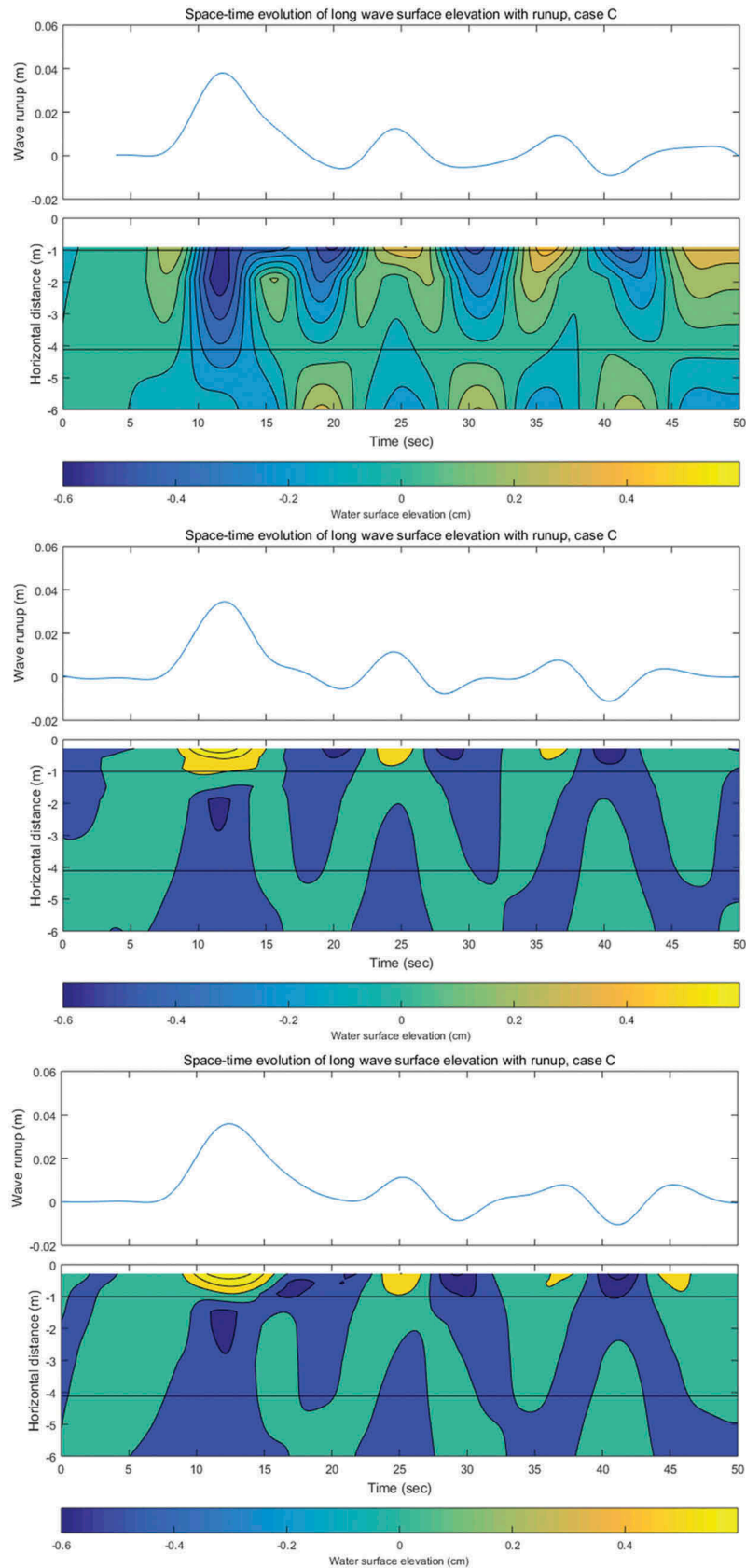


Figure 13. Time series of low-frequency component of wave run-up and space-time evolution of low-frequency surface elevation of experiment (top), OpenFOAM (middle) and COULWAVE (bottom) of case C. Horizontal blue line indicate the bottom slope changes.

OpenFOAM. The predictions of the maximum wave run-ups are in close agreement with the correlation line which means perfect agreement with the experiments.

The generation of long wave by the shoaling and breaking of the propagation of top-hat spectral waves, a transient-focused wave group, over composite slopes by using HCW was investigated. The time

series of water surface elevation and the amplitude spectra by the laboratory observations were compared with numerical simulations, OpenFOAM and COULWAVE, based on Boussinesq and RANS equations, respectively. The comparisons show that long wave generation in the experiments is in close agreement with numerical simulations. The time series of water surface elevations shows that the short wave groups are transformed to long waves, and their propagation paths can be observed directly. In addition, the comparison of the amplitude spectra presents that the primary and superharmonic wave amplitudes are increased or decreased by wave shoaling or wave breaking, respectively. Long wave components obtained from low-pass filtered surface elevations by time-series measurement obviously describe that the increased amplitudes in shallow water by shoaling and their propagation path. The wave amplitude spectra measured and predicted were compared to the second-order wave theory in association with an interaction of wave groups Longuet-Higgins and Stewart (1960). The comparisons of the theory at initial location and experimental data and numerical results at various cross shore locations present that a spatial redistribution of wave energy is obviously described during the shoaling and breaking processes. The wave amplitude spectra with low-frequency increase over nearshore regions because the wave amplitudes with low-frequency become increased in shallow water due to wave shoaling and the energy is transferred from the waves with higher frequency.

In the cases of top-hat spectral waves, moreover, the time series of inundations and wave run-ups for all cases measured and predicted with COULWAVE and OpenFOAM have discrepancies because the wave conditions before wave run-up are different as well. However, the tendencies of wave run-ups and rundowns are so close between the measurements and the predictions. In detail, the sequence of wave run-ups by the bound long waves can be observed. In addition, the time series of run-ups with high resolutions including wave run-ups and rundown with high frequencies can be observed.

To investigate the space-time evolution of wave transformation and run-up, the contour plots of surface elevation and time series of wave run-up by the laboratory observation and the model predictions. The paths of wave group propagating with highly non-linear motion on the composite slope can be presented. The space-time evolution of low-frequency component ($f_c < 0.4$) of surface elevation and the time series of wave run-up by the laboratory observation and the model predictions is illustrated. The bound long wave is amplified by shoaling after passing the first slope and that the subsequent wave run-ups are dominated

by the reflected bound long wave. In addition, the positive surges in advance of bound long wave trough lead a low-frequency run-up on the composite slope.

Disclosure statement

No potential conflict of interest was reported by the authors.

ORCID

Haeng Sik Ko  <http://orcid.org/0000-0002-1744-8878>

Patrick J. Lynett  <http://orcid.org/0000-0002-2856-9405>

References

- Baldock, T. 2006. "Long Wave Generation by the Shoaling and Breaking of Transient Wave Groups on a Beach." In *Proceedings of the Royal Society of London A: Mathematical, Physical and Engineering Sciences* 462: 1853–1876.
- Baldock, T. E., C. Swan, and P. H. Taylor 1996. "A Laboratory Study of Nonlinear Surface Waves on Water." In *Proceedings of the Royal Society of London A: Mathematical, Physical and Engineering Sciences* 354: 649–676. doi:10.1098/rsta.1996.0022.
- Battjes, J. 1974. "Surf Similarity." *Coastal Engineering Proceedings* 1 (14): 466–480.
- Bouquet, J. Y. 1999. "Visual Methods for Three-Dimensional Modeling." PhD dissertation, Caltech.
- Canny, J. 1986. "A Computational Approach to Edge Detection." *IEEE Transactions on Pattern Analysis and Machine Intelligence* PAMI-8 (6): 679–698. doi:10.1109/TPAMI.1986.4767851.
- Daily, J., and S. C. Stephan. 1952. "The Solitary Wave: Its Celerity, Profile, Internal Velocities and Amplitude Attenuation in a Horizontal Smooth Channel." *Coastal Engineering Proceedings* 1 (3): 13–29.
- Guza, R. T., and E. B. Thornton. 1982. "Swash Oscillations on a Natural Beach." *Journal of Geophysical Research: Oceans* 87 (C1): 483–491. doi:10.1029/JC087iC01p00483.
- Hofland, B., E. Diamantidou, P. van Steeg, and P. Meys. 2015. "Wave Runup and Wave Overtopping Measurements Using a Laser Scanner." *Coastal Engineering* 106: 20–29. doi:10.1016/j.coastaleng.2015.09.003.
- Holland, K. T., R. A. Holman, T. C. Lippmann, J. Stanley, and N. Plant. 1997. "Practical Use of Video Imagery in Nearshore Oceanographic Field Studies." *IEEE Journal of Oceanic Engineering* 22 (1): 81–92. doi:10.1109/48.557542.
- Hunt, A. 2003. "Extreme Waves, Overtopping and Flooding at Sea Defences." PhD dissertation, University of Oxford.
- Hunt, I. A. 1959. "Design of Sea-Walls and Breakwaters." *Transactions of the American Society of Civil Engineers* 126 (4): 542–570.
- Kalligeris, N., V. Skanavis, S. Tavakkol, A. Ayca, H. E. Safty, P. Lynett, and C. E. Synolakis. 2016. "Lagrangian Flow Measurements and Observations of the 2015 Chilean Tsunami in Ventura, Ca." *Geophysical Research Letters* 43 (10): 5217–5224. doi:10.1002/2016GL068796.
- Kânođlu, U., and C. E. Synolakis. 1998. "Long Wave Runup on Piecewise Linear Topographies." *Journal of Fluid Mechanics* 374: 1–28. doi:10.1017/S0022112098002468.

- Kaur, S., and I. Singh. 2016. "Comparison between Edge Detection Techniques." *International Journal of Computer Applications* 145 (15): 15–18. doi:10.5120/ijca2016910867.
- Ko, H., and P. Lynett. 2014. "Development of a Hydraulic-Control Wave-Maker (Hcw) for the Study of Combined Waves and Flows." *Coastal Engineering Proceedings* 1 (34): waves.53. doi:10.9753/icce.v34.waves.53.
- Ko, H. S., Y. H. Bae, and I. H. Cho. 2018. "Dynamic Analysis of a Floating Structure Using OpenFOAM." *Journal of Computational Fluids Engineering* 23 (1): 101–112. doi:10.6112/kscfe.2018.23.1.101.
- Kobayashi, N., G. S. DeSilva, and K. D. Watson. 1989. "Wave Transformation and Swash Oscillation on Gentle and Steep Slopes." *Journal of Geophysical Research: Oceans* 94 (C1): 951–966. doi:10.1029/JC094iC01p00951.
- Lara, J. L., A. Ruju, and I. J. Losada. 2010. "Reynolds Averaged Navier–Stokes Modelling of Long Waves Induced by a Transient Wave Group on a Beach." *Proceedings of the Royal Society of London A: Mathematical, Physical and Engineering Sciences* 467: 1215–1242.
- Li, Y., and F. Raichlen. 2001. "Solitary Wave Runup on Plane Slopes." *Journal of Waterway, Port, Coastal, and Ocean Engineering* 127 (1): 33–44. doi:10.1061/(ASCE)0733-950X(2001)127:1(33).
- Liu, P.-F. 1994. "Model Equations for Wave Propagation from Deep to Shallow Water." *Advances in Coastal Engineering* 1: 125–157.
- Longuet-Higgins, M. S., and R. W. Stewart. 1960. "Changes in the Form of Short Gravity Waves on Long Waves and Tidal Currents." *Journal of Fluid Mechanics* 8: 565–583. doi:10.1017/S0022112060000803.
- Lynett, P. J., T.-R. Wu, and P.-F. Liu. 2002. "Modeling Wave Runup with Depth-Integrated Equations." *Coastal Engineering* 46 (2): 89–107. doi:10.1016/S0378-3839(02)00043-1.
- Madsen, P., and O. Sorensen. 1992. "A New Form of the Boussinesq Equations with Improved Linear Dispersion Characteristics. Part 2. A Slowly-Varying Bathymetry." *Coastal Engineering* 18: 183–204. doi:10.1016/0378-3839(92)90019-Q.
- Nwogu, O. 1993. "Alternative Form of Boussinesq Equations for Nearshore Wave Propagation." *Journal of Waterway, Port, Coastal, and Ocean Engineering* 119 (6): 618–638. doi:10.1061/(ASCE)0733-950X(1993)119:6(618).
- Pedersen, G. K., E. Lindstrøm, A. F. Bertelsen, A. Jensen, D. Laskovski, and G. Sælevik. 2013. "Runup and Boundary Layers on Sloping Beaches." *Physics of Fluids* 25 (1): 012102. doi:10.1063/1.4773327.
- Rapp, R. J., and W. K. Melville. 1990. "Laboratory Measurements of Deep-Water Breaking Waves." *Proceedings of the Royal Society of London A: Mathematical, Physical and Engineering Sciences* 331 (1622): 735–800.
- Sælevik, G., A. Jensen, and G. Pedersen. 2013. "Runup of Solitary Waves on a Straight and a Composite Beach." *Coastal Engineering* 77: 40–48. doi:10.1016/j.coastaleng.2013.02.007.
- Stokes, G. G. 1847. "On the Theory of Oscillatory Waves." *Transactions of the Cambridge Philosophical Society* 8: 441–455.
- Synolakis, C. E. 1987. "The Runup of Solitary Waves." *Journal of Fluid Mechanics* 185: 523–545. doi:10.1017/S002211208700329X.
- Versteeg, H., and W. Malalasekera. 2007. *An Introduction to Computational Fluid Dynamics: The Finite Volume Method*. UK: Pearson Education Limited.
- Wei, G., J. T. Kirby, S. T. Grilli, and R. Subramanya. 1995. "A Fully Nonlinear Boussinesq Model for Surface Waves. Part 1. Highly Nonlinear Unsteady Waves." *Journal of Fluid Mechanics* 294: 71–92. doi:10.1017/S0022112095002813.
- Weller, H. G., G. Tabor, H. Jasak, and C. Fureby. 1998. "A Tensorial Approach to Computational Continuum Mechanics Using Object-Oriented Techniques." *Computers in Physics* 12: 620–631. doi:10.1063/1.168744.

Appendix A

Coefficients of Second-Order Solution:

$$C = \frac{[2\sigma_1\sigma_2(\sigma_1 - \sigma_2)(1 + a_1a_2) + \sigma_1^3(a_1^2 - 1) - \sigma_2^3(a_2^2 - 1)](\sigma_1 - \sigma_2)(a_1a_2 - 1)}{\sigma_1^2(a_1^2 - 1) - 2\sigma_1\sigma_2(a_1a_2 - 1) + \sigma_2^2(a_2^2 - 1)} \quad (\text{A.1})$$

$$= +(\sigma_1^2 + \sigma_2^2) - \sigma_1\sigma_2(a_1a_2 + 1)$$

$$D = \frac{[2\sigma_1\sigma_2(\sigma_1 + \sigma_2)(a_1a_2 - 1) + \sigma_1^3(a_1^2 - 1) + \sigma_2^3(a_2^2 - 1)](\sigma_1 + \sigma_2)(a_1a_2 - 1)}{\sigma_1^2(a_1^2 + 1) - 2\sigma_1\sigma_2(a_1a_2 + 1) + \sigma_2^2(a_2^2 - 1)} \quad (\text{A.2})$$

$$= -(\sigma_1^2 + \sigma_2^2) + \sigma_1\sigma_2(a_1a_2 - 1)$$

$$E = -\frac{1}{2}a_1a_2[2\sigma_1\sigma_2(\sigma_1 - \sigma_2)(1 + a_1a_2) + \sigma_1^3(a_1^2 - 1) - \sigma_2^3(a_2^2 - 1)] \quad (\text{A.3})$$

$$F = -\frac{1}{2}a_1a_2[2\sigma_1\sigma_2(\sigma_1 + \sigma_2)(1 - a_1a_2) - \sigma_1^3(a_1^2 - 1) - \sigma_2^3(a_2^2 - 1)] \quad (\text{A.4})$$

where a coefficients are $a_1 = \coth(k_1h)$ and $a_2 = \coth(k_2h)$.